

# 1 Spectrometric measurements of atmospheric propane (C<sub>3</sub>H<sub>8</sub>)

2 Geoffrey C. Toon<sup>1</sup>, Jean-Francois L. Blavier<sup>1</sup>, Keeyoon Sung<sup>1</sup>, Katelyn Yu<sup>1,2</sup>

3 <sup>1</sup> Jet Propulsion Laboratory, California Institute of Technology, Pasadena, CA, 91109, USA

4 <sup>2</sup> Dept. Civil and Environmental Engineering, UC Berkeley, Berkeley, CA, 94720, USA

5 Correspondence to: Geoffrey.C.Toon@jpl.nasa.gov

6 **Abstract.** We report measurements of atmospheric C<sub>3</sub>H<sub>8</sub> from analysis of ground-based, solar absorption spectra  
7 from the JPL MkIV interferometer. Using the strong Q-branch absorption feature at 2967 cm<sup>-1</sup>, we can measure  
8 C<sub>3</sub>H<sub>8</sub> in locations where its abundance is enhanced by proximity to sources (e.g., large natural gas fields, mega-  
9 cities). A case study of MkIV C<sub>3</sub>H<sub>8</sub> measurements from Ft. Sumner, New Mexico, shows that amounts are strongly  
10 correlated with ethane (C<sub>2</sub>H<sub>6</sub>) and with back-trajectories from SE New Mexico and West Texas, where the Permian  
11 Basin oil and natural gas field is located. Measurements from JPL, California, also show large C<sub>3</sub>H<sub>8</sub> enhancements  
12 on certain days, but more correlated with CO than C<sub>2</sub>H<sub>6</sub>. ~~From high-altitude, balloon-borne, MkIV solar occultation~~  
13 ~~measurements, C<sub>3</sub>H<sub>8</sub> was not detected at any altitude (5-40 km) in any of its 25 flights.~~

## 14 1. Introduction

15 Non-methane hydrocarbons such as C<sub>3</sub>H<sub>8</sub> and C<sub>2</sub>H<sub>6</sub> affect air quality because their oxidation enhances tropospheric  
16 O<sub>3</sub> and aerosol pollution. They are also sensitive indicators of fugitive losses by the oil and natural gas industry, an  
17 important source of co-emitted methane (CH<sub>4</sub>), a greenhouse gas. These fugitive losses appear to be under-  
18 estimated in global inventories (Dalsoren et al., 2018).

19 Atmospheric C<sub>3</sub>H<sub>8</sub> and C<sub>2</sub>H<sub>6</sub> are entirely the result of emissions at the surface. In pre-industrial times these came  
20 from geological seeps and wild fires, but in recent times these natural sources have been surpassed by emissions  
21 from fossil fuel production. The latter peaked in about 1970, and then declined due to stricter regulation of  
22 emissions from the oil and natural gas industry and automobiles. But in the past decade, this decreasing trend has  
23 reversed due to accelerated Natural Gas (NG) exploitation (Helmig et al., 2016).

24 C<sub>3</sub>H<sub>8</sub> has a lifetime of about 2 weeks in summer and 8 weeks in winter (Rosado-Reyes et al., 2007). This is mostly  
25 dictated by how fast it is being oxidized by reactions with hydroxyl radicals and chlorine atoms. Given this 2–8  
26 week lifetime, a single strong source of propane has the potential to degrade air quality over most of the hemisphere.

27 Unprocessed, in-the-ground, “wet” natural gas is usually between 70–95% CH<sub>4</sub>, 1–15% C<sub>2</sub>H<sub>6</sub>, 1–10% C<sub>3</sub>H<sub>8</sub>, and 0–  
28 3% C<sub>4</sub>H<sub>10</sub>. The latter two gases are typically extracted to form Liquefied Petroleum Gas (LPG). In the northern  
29 hemisphere winter, LPG contains more C<sub>3</sub>H<sub>8</sub>, while in summer it contains more butane (C<sub>4</sub>H<sub>10</sub>), reducing variations  
30 in its vapor pressure.

Deleted: large variations

Deleted: amounts

Formatted: Font: Times New Roman, 10 pt

Deleted: From MkIV solar occultation measurements from balloon, C<sub>3</sub>H<sub>8</sub> was not detected at any altitude in any flight

Formatted: Font: Times New Roman, 10 pt, Subscript

Formatted: Font: Times New Roman, 10 pt

Formatted: Font: Times New Roman, 10 pt

Formatted: Font: Times New Roman, 10 pt, Subscript

Formatted: Font: Times New Roman, 10 pt

Moved down [1]: In contrast, the lifetime of C<sub>2</sub>H<sub>6</sub> is 2–6 months, which is 3–4 times longer than that of C<sub>3</sub>H<sub>8</sub>.

Moved (insertion) [1]

Deleted: In contrast, the lifetime of C<sub>2</sub>H<sub>6</sub> is 2–6 months, which is 3–4 times longer than that of C<sub>3</sub>H<sub>8</sub>.

39 LPG burns much more cleanly than fuel oil and is therefore increasingly used for heating, and cooking, especially in  
40 rural areas that are not served by piped NG. LPG is also used to fuel commercial vehicles, and is increasingly  
41 replacing CFCs as a refrigerant and as an aerosol propellant. As a result of extracting LPG from natural gas, the NG  
42 that is piped to our homes in urban areas is highly depleted in C<sub>3</sub>H<sub>8</sub> and C<sub>4</sub>H<sub>10</sub>, as compared with wet NG.

Deleted: is

43 To the best of our knowledge, there are no previous remote sensing measurements of C<sub>3</sub>H<sub>8</sub>, although in situ  
44 measurements exist. Dalsoren et al. (2018, Fig.3b) show surface in situ C<sub>3</sub>H<sub>8</sub> amounts below 50 ppt at Zeppelin  
45 station in Svalbad in summer 2011, but with values of 1 ppb in the winter, with peaks of up to 2.4 ppb. These C<sub>3</sub>H<sub>8</sub>  
46 peaks are strongly correlated with C<sub>2</sub>H<sub>6</sub> which reaches 3.4 ppb. Using in situ C<sub>3</sub>H<sub>8</sub> data from multiple sites Helmig et  
47 al. (2016) show a large seasonal cycle in surface in situ C<sub>3</sub>H<sub>8</sub> at high NH latitudes, reaching 1 ppb in winter, with  
48 little in the SH. They also show increasing C<sub>3</sub>H<sub>8</sub> over central and Eastern US over the period 2009.5–2014.5, but no  
49 increase on the West coast.

Deleted: report

Deleted: of essentially zero

Deleted: a

50 Since C<sub>3</sub>H<sub>8</sub> correlates with C<sub>2</sub>H<sub>6</sub>, both having NG as their main source, we also consider the previous measurements  
51 of C<sub>2</sub>H<sub>6</sub>, which has a lifetime of 2-8 months, 4 times longer than propane. Angelbratt et al. (2011) reported a 0–  
52 2%/year decline over the period 1996 to 2006 based on data from six NH FTIR sites. Franco et al (2015) reported a  
53 shallow minimum in C<sub>2</sub>H<sub>6</sub> in the 2005–2010 period based on ground-based FTIR solar spectra above the  
54 Jungfraujoch scientific station. Helmig et al. (2016) report a minimum in atmospheric C<sub>2</sub>H<sub>6</sub> in 2005–2010 based on  
55 in situ and remote measurements.

Deleted: .

56 Franco et al. (2016) estimate a 75% increase in North American C<sub>2</sub>H<sub>6</sub> emissions between 2008 and 2014, and as a  
57 result report a 3–5% annual increase in column C<sub>2</sub>H<sub>6</sub> at Northern mid latitudes. They hypothesize that this increase  
58 is the result of the recent massive growth in the exploitation of shale gas and tight oil reservoirs in North America,  
59 where the drilling productivity began to grow rapidly after 2009.

## 60 2. Methods

### 61 2.1 MkIV Instrument

62 The JPL MkIV interferometer (Toon, 1991) is a high-resolution FITR spectrometer built at JPL in 1984. It covers  
63 the entire 650–5650 cm<sup>-1</sup> range simultaneously in every spectrum with two detectors: a HgCdTe photoconductor  
64 covering 650–1800 cm<sup>-1</sup> and an InSb photodiode covering 1800–5650 cm<sup>-1</sup>. For ground-based observations a  
65 maximum OPD of 117 cm is employed providing a spectral resolution of 0.005 cm<sup>-1</sup>. The MkIV is primarily a  
66 balloon instrument and has performed 25 flights since 1989, the latest in 2019. Between balloon flights it makes  
67 ground-based observations. Since 1985 it has taken 5000 ground-based observations on 1200 different days from 12  
68 different sites. For more detail, see tables in: <https://mark4sun.jpl.nasa.gov/ground.html>

Deleted: K

Deleted: K

### 69 2.2 Retrieval

77 The analysis of the MkIV spectra was performed with the GFIT (Gas Fitting) tool, a nonlinear, least-squares,  
78 spectral-fitting, algorithm developed at JPL. GFIT has been previously used for the Version 3 analysis (Irion et al.,  
79 2002) of spectra measured by the Atmospheric Trace Molecule Occultation Spectrometer, and it is currently used for  
80 analysis of Total Carbon Column Observing Network (TCCON) spectra (Wunch et al., 2011) and for MkIV spectra  
81 (Toon et al., 2016; 2018a; 2018b). The entire package including spectral fitting software, spectroscopic line lists, and  
82 software to generate a priori VMR/T/P profiles, is termed GGG.

Deleted: K

Deleted: 3

83 GFIT scales the atmospheric gas volume mixing ratio (VMR) profiles to fit calculated spectra to those measured.  
84 For C<sub>3</sub>H<sub>8</sub>, a 5.4 cm<sup>-1</sup>-wide fitting window centered on the Q-branch at 2967 cm<sup>-1</sup> was used. The atmosphere was  
85 discretized into 70 layers of 1 km thickness. C<sub>3</sub>H<sub>8</sub> and four interfering gases (H<sub>2</sub>O, CH<sub>4</sub>, C<sub>2</sub>H<sub>6</sub>, HDO) were adjusted.  
86 Two frequency stretches were retrieved (telluric and solar). The spectral continuum was fitted as a straight line, and  
87 a zero-level offset was fitted. So that's a total of 10 simultaneously-fitted scalars. In addition, the solar pseudo-  
88 transmittance was computed (but not adjusted).

89 The assumed temperature, pressure and H<sub>2</sub>O profiles were based on the NCEP 6-hourly analyses for solar noon of  
90 each day. The a priori vmr profiles were based on NH mid-latitude profiles. This is the same scheme as used by the  
91 GGG TCCON analysis (Wunch et al., 2015), but here we apply it to the Mid-IR MkIV spectra rather than the Short-  
92 Wave IR TCCON spectra.

Deleted: exactly

Deleted: 2014

Deleted: W

93 To estimate the sensitivity of the retrieved C<sub>3</sub>H<sub>8</sub> to uncertainties in the assumed a priori profiles of T/P and  
94 interfering gases (especially H<sub>2</sub>O, CH<sub>4</sub>), we retrieve the post-2000 C<sub>3</sub>H<sub>8</sub> a second time: using GGG2020, an updated  
95 version of the GGG code with improved a priori VMR/T/P profiles based on the GEOS-FP-IT analysis (Laughner et  
96 al., 2021). The results, shown in figure B.2, illustrate that this changes the retrieved C<sub>3</sub>H<sub>8</sub> by less than 10% with a  
97 bias of only 1.1%.

Deleted: instead of GGG2014

Deleted: appendix

Deleted: A

Deleted: show

Deleted: rms

Deleted: lab

Formatted: Font color: Text 1

Formatted: Font: Times New Roman, 10 pt, Not Italic, Font color: Text 1

Formatted: Font color: Text 1

Formatted: Font: Times New Roman, 10 pt, Not Italic, Font color: Text 1

### 98 2.3. Spectroscopy

99 It is clear from the infra-red lab spectrum of C<sub>3</sub>H<sub>8</sub> (Fig.1), measured at Pacific North-West National Laboratory  
100 (Sharpe et al., 2004), that the feature at 2967 cm<sup>-1</sup>, caused by various CH<sub>2</sub> and CH<sub>3</sub> stretch vibrational modes, is by  
101 far the strongest in the entire infrared. So for solar occultation spectrometry, this is by far the best choice. For  
102 thermal emission spectrometry from cold planets such as Titan, however, these bands are not covered by  
103 Cassini/CIRS since the thermal Plank function of such planets weakens rapidly above 2000 cm<sup>-1</sup>. Thus, the much  
104 weaker bands below 1400 cm<sup>-1</sup> must be used (Sung et al., 2013).

Deleted: . For thermal emission spectrometry from cold planets such as Titan, on the other hand, then the much weaker CH<sub>3</sub> deform bands around 1400 cm<sup>-1</sup> would be better (Sung et al., 2013).

Formatted: Font: 10 pt

Formatted: Superscript

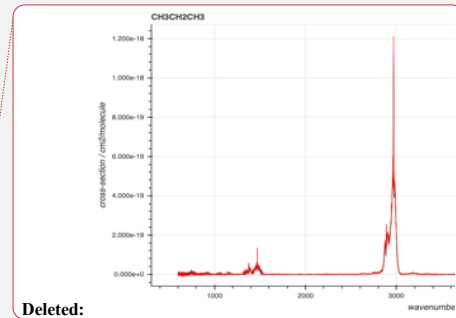
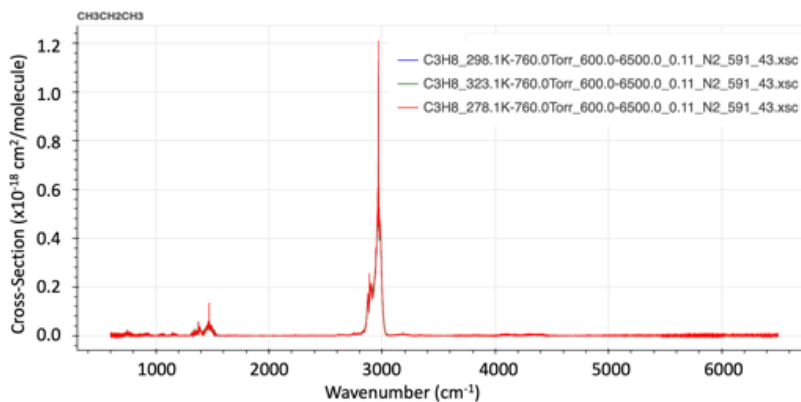
Formatted: Font: 10 pt

Formatted: Font: 10 pt, Superscript

Formatted: Font: 10 pt

Formatted: Font: 10 pt

Formatted: Font: 10 pt



Deleted:

120

121 **Figure 1.** Infrared spectra of PNNL  $C_3H_8$  absorption cross-section at 323, 298, and 278K (from hitran.org).

Deleted: laboratory

Formatted: Font: Italic

122 An empirical pseudo-line-list (EPLL) of  $C_3H_8$  covering 2560–3280  $cm^{-1}$  was derived from the laboratory cross-  
 123 sections of Harrison and Bernath (2010b). This is described in the unpublished report:

124 [https://mark4sun.jpl.nasa.gov/data/spec/Pseudo/c3h8\\_pll\\_2560\\_3280.pdf](https://mark4sun.jpl.nasa.gov/data/spec/Pseudo/c3h8_pll_2560_3280.pdf)

125 The use of an EPLL facilitates interpolation and extrapolation of the lab cross-sections to T/P conditions that were  
 126 not measured in the lab. The fitting of the EPLL also checks the self-consistency of the lab cross-section spectra,  
 127 and provides an opportunity to correct for artifacts in the lab spectra (e.g., channeling, zero-level offsets,  
 128 contamination, ILS), although it must be stated that in this particular case the  $C_3H_8$  lab spectra were of very high  
 129 quality and comprehensive in terms of their coverage. For the interfering  $C_2H_6$ , an EPLL developed eight years ago  
 130 was used, based on lab measurements of Harrison et al. (2010a), as described in the report:

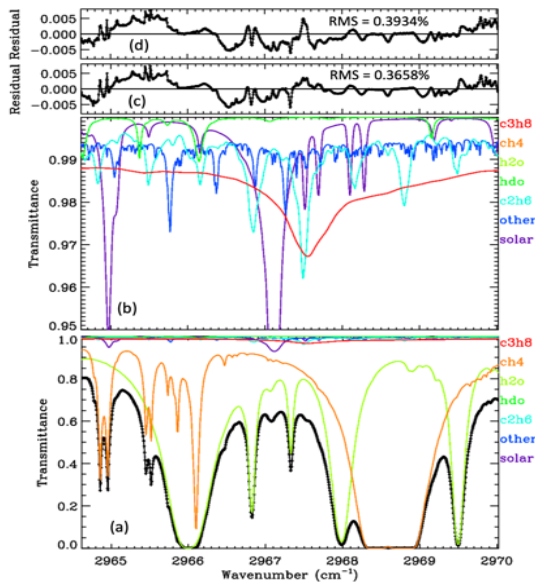
131 [https://mark4sun.jpl.nasa.gov/report/C2H6\\_spectroscopy\\_evaluation\\_2850-3050\\_cm-1.compressed.pdf](https://mark4sun.jpl.nasa.gov/report/C2H6_spectroscopy_evaluation_2850-3050_cm-1.compressed.pdf)

132 For other gases the atm.161 linelist was used, which is based on HITRAN 2016, with some empirical adjustments  
 133 based on fits to lab spectra, especially for  $H_2O$  and  $CH_4$ . This is basically the same linelists (atm.161, pll.101) that  
 134 are used by TCCON, but here we use them in the MIR rather than the SWIR.

135 Figure 2 shows an average spectral fit to the  $C_3H_8$  window in ground-based MkIV spectra, obtained by fitting  
 136 individual spectra and then averaging the results. The lower panel provides the full transmittance y-range from 0 to  
 137 1. It can be seen that the main absorbers are  $CH_4$  (orange) and  $H_2O$  (green). The  $C_3H_8$  absorption (red) is difficult to  
 138 discern because it is so shallow. The lower-middle panel shows the same spectral fit, but with the y-scale zoomed  
 139 into 0.95–1.00 transmittance, allowing the weak absorbers like  $C_3H_8$  and  $C_2H_6$  to be more easily seen. The “other”  
 140 contributions (e.g.,  $O_3$ ) were included in the calculation but not adjusted. The  $C_3H_8$  absorption is fairly flat at about  
 141 1% depth, except for the Q-branch where it deepens to 2½%. Although the strongest  $C_2H_6$  feature coincides with the  
 142  $C_3H_8$  Q-branch, the former is much narrower and there are several additional  $C_2H_6$  features in this window, so the

Deleted: we expect little

146 spectrometric “cross-talk” between these two gases should be modest; we compute a Pearson Correlation  
 147 Coefficient of -0.7 between the  $C_2H_8$  and  $C_2H_6$ . Further discussion on this topic can be found in Appendix A. The  
 148 upper-middle panel shows that the residuals (measured-calculated transmittance) have some systematic features of  
 149 ~0.5% in magnitude, especially in the vicinity of the  $H_2O$  line at  $2966.0\text{ cm}^{-1}$ . The topmost panel shows the  
 150 residuals to a fit performed without any  $C_3H_8$  absorption lines. It looks surprisingly similar to the fit performed with  
 151  $C_3H_8$  lines, such is the ingenuity of the spectral fitting algorithm in adjusting the  $H_2O$ ,  $CH_4$ , and  $C_2H_6$  to compensate  
 152 for the missing  $C_3H_8$ . The overall RMS residual in the no- $C_3H_8$  case is 0.3934%, as compared with 0.3658% when  
 153  $C_3H_8$  is included. This is quite significant considering that residuals are dominated by the  $H_2O$  line at  $2966.0\text{ cm}^{-1}$ ,  
 154 and are unaffected by whether  $C_3H_8$  is included or not. The residuals in the topmost panel (d) are larger in the  
 155 vicinity of the  $C_3H_8$  Q-branch,  $2967\text{-}2968\text{ cm}^{-1}$  than those in panel (c).



156  
 157 **Figure 2.** The average of 5000 ground-based MkIV spectral fits. Black diamonds represent measured spectrum.  
 158 Black line the fitted calculation. Colored lines represent the contributions of different gases. Panel (a) shows the full  
 159 transmittance range. Panel (b) zooms into the 0.95–1.00 range to help see the weak absorbers ( $C_2H_6$ ,  $HDO$ , and the  
 160 solar lines). Panel (c) show residuals (Measured-Calculated); these are generally below 0.5%. Panel (d) shows the  
 161 residuals when  $C_3H_8$  is excluded from the calculation.

162 Considering the weakness (and smoothness) of the  $C_3H_8$  Q-branch in comparison with the residuals and the  
 163 contributions of the other gases, we were at first skeptical that a useful  $C_3H_8$  column measurement could be

Deleted: .  
 Formatted: Subscript  
 Formatted: Subscript  
 Formatted: Subscript  
 Formatted: Subscript  
 Deleted: top  
 Formatted: Subscript  
 Formatted: Subscript  
 Formatted: Subscript  
 Formatted: Subscript  
 Formatted: Subscript  
 Formatted: Subscript  
 Formatted: Subscript  
 Formatted: Subscript  
 Formatted: Subscript  
 Formatted: Subscript  
 Formatted: Subscript  
 Formatted: Subscript  
 Formatted: Subscript  
 Formatted: Subscript  
 Formatted: Subscript  
 Formatted: Subscript  
 Formatted: Subscript  
 Formatted: Subscript  
 Formatted: Subscript  
 Formatted: Subscript  
 Formatted: Subscript  
 Formatted: Subscript  
 Formatted: Subscript  
 Formatted: Subscript  
 Formatted: Subscript  
 Formatted: Subscript  
 Formatted: Subscript  
 Deleted: Considering the weakness (and smoothness) of the  $C_3H_8$  Q-branch in comparison with the residuals and the contributions of the other gases, we were at first skeptical that a useful  $C_3H_8$  column measurement could be extracted from such spectral fits. But since the analysis of the MkIV spectra is highly automated, it took only a few hours to run the  $C_3H_8$  window shown in Fig.2 over the 5000 MkIV ground-based spectra.  
 Deleted: → →  
 Deleted: Bottom p  
 Deleted: Middle p  
 Deleted: Top p  
 Formatted: Subscript  
 Formatted: Subscript

182 extracted from such spectral fits. But since the analysis of the MkIV spectra is highly automated, it took only a few  
 183 hours to run the C<sub>3</sub>H<sub>8</sub> window over all 5000 MkIV ground-based spectra.

184

### 185 3. Results

186 Table 1 lists the observation sites from where MkIV has made ground-based observations up to the end of 2019. The  
 187 vast majority are from three sites: JPL, Mt. Barcroft, and Ft. Sumner.

188

Town	State	N <sub>obs</sub>	N <sub>day</sub>	Latitude (deg.)	Longitude (deg.)	Altitude (km)	Terrain	Years Operated
Estrange	Sweden	160	32	67.889	+21.085	0.271	Boreal	1999–2007
Fairbanks	Alaska	124	46	64.830	-147.614	0.182	Boreal	1997
Lynn Lake	Manitoba	20	11	56.858	-101.066	0.354	Boreal	1996
Mt. Barcroft	California	1369	258	37.584	-118.235	3.801	Alpine	1994–2002
Mtn. View	California	7	4	37.430	-122.080	0.010	Urban	1987, 2001
Daggett	California	33	21	34.856	-116.790	0.626	Desert	1993
Ft. Sumner	New Mex.	521	106	34.480	-104.220	1.260	Steppe	1989–2019
TMF	California	475	45	34.382	-117.678	2.257	Alpine	1986–2009
JPL (B183)	California	2273	690	34.199	-118.174	0.345	Urban	1985–2020
JPL (mesa)	California	20	5	34.205	-118.171	0.460	Urban	1988–1989
Palestine	Texas	4	3	31.780	-95.700	0.100	Rural	1989
McMurdo	Antarctica	37	20	-77.847	+166.728	0.100	Polar	1986

Formatted Table

Formatted: Font color: Text 1

Formatted: Font color: Text 1

Formatted: Font color: Text 1

Formatted: Font color: Text 1

189

190 **Table 1.** The twelve sites from where MkIV has made ground-based observations, along with the number of  
 191 observations and observation days from each, years of operations, their location, and terrain type. They greyed out  
 192 sites have the fewest observations (only 1% of total) and are not included in the Figures 5-7 and A.1 to reduced  
 193 color ambiguity.

Formatted: Font: Bold, Italic

Formatted: Font: Italic

Formatted: Font: Italic

Formatted: Font: Italic

194 Fig. 3 shows MkIV ground-based C<sub>3</sub>H<sub>8</sub> columns, color coded by site altitude. The data were filtered: only points  
 195 with uncertainties < 1.5x10<sup>16</sup> were plotted, reducing the number of plotted points from 5000 to 4700. The top panel  
 196 (a) shows that at the high-altitude sites (Mt. Barcroft at 3.8 km is Red; Table Mountain Facility at 2.26 km is  
 197 Orange) the retrieved C<sub>3</sub>H<sub>8</sub> columns are centered around zero. Also, the data acquired in Sep 1986 from 0.1 km in  
 198 Antarctica (dark blue) are also centered around zero. Data acquired from Ft. Sumner, NM, at 1.2 km (lime) have  
 199 large variations, from zero to nearly 8x10<sup>16</sup> molecules.cm<sup>-2</sup>, as do the data from JPL at 0.35 km (cyan). Other sites  
 200 with detectable C<sub>3</sub>H<sub>8</sub> include Daggett, CA, (0.6km), Estrange, Sweden (0.26km) in the winter, Fairbanks, AK  
 201 (0.2km), and Mountain View, CA in late 1991. So C<sub>3</sub>H<sub>8</sub> has only been measured by MkIV from northern  
 202 hemisphere sites within the PBL. Panels (b) and (c) show the same C<sub>3</sub>H<sub>8</sub> columns, but plotted versus year and day.

Deleted: 5E+

Deleted: =

Deleted: =

Deleted: E+

Moved (insertion) [2]

Moved up [2]: So C<sub>3</sub>H<sub>8</sub> has only been measured by MkIV from northern hemisphere sites within the PBL.

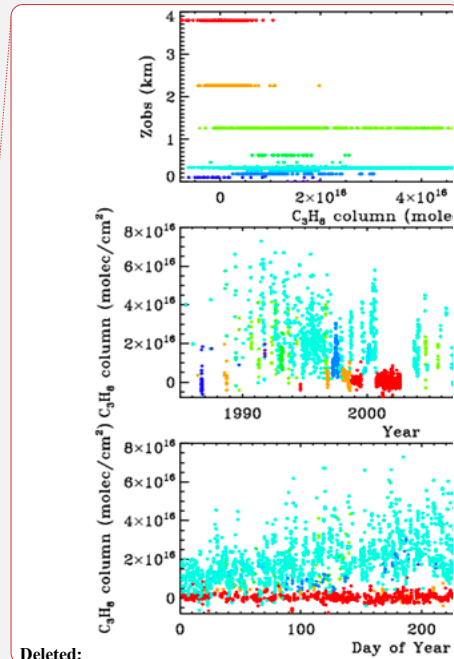
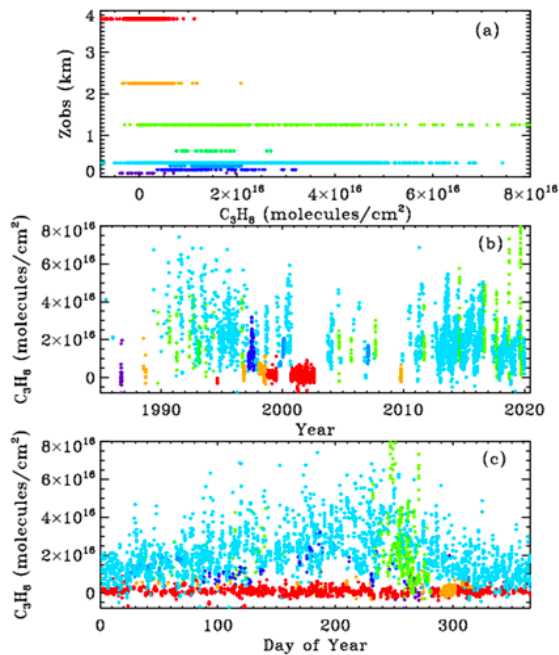
Formatted: Superscript

Deleted: , probably

Deleted: ing

203 High C<sub>3</sub>H<sub>8</sub> values (>4x10<sup>16</sup> molecules.cm<sup>-2</sup>) can occur at any time of year at JPL (cyan) but most commonly in late  
 204 summer, as is the case for other pollutants, e.g. CO. This reflects the meteorology (stagnant conditions in the LA

213 basin in summer with little replacement of polluted air with clean air from outside). Averaging kernels for these  
 214 C<sub>3</sub>H<sub>8</sub> measurements are discussed and illustrated in Appendix B. Suffice it to say here that they range from 0.9 to  
 215 1.4 and increase with altitude.



216

217 **Figure 3.** MklV C<sub>3</sub>H<sub>8</sub> column abundances from 8/12 sites, color-coded by site altitude, as illustrated in panel (a):  
 218 *Violet=0.1 km (McMurdo); dark blue=0.18 km (Fairbanks); light blue=0.27 km (Esrange); cyan=0.35 km (JPL);*  
 219 *Green=0.63 km (Daggett); lime=1.2 km (Ft. Sumner); orange=2.2 km (TMF); red=3.8 km (Mt. Barcroft).*

Deleted: all

Deleted: blue

Deleted: 0

Deleted: 5

220 The reported uncertainties in our C<sub>3</sub>H<sub>8</sub> column measurements are based on the rms fitting residuals compared with  
 221 the sensitivity of the spectrum to C<sub>3</sub>H<sub>8</sub> (Jacobians). At the highest site, Barcroft at 3.8 km (P=0.65 atm.), where the  
 222 interfering H<sub>2</sub>O and CH<sub>4</sub> absorptions are relatively weak and narrow, the C<sub>3</sub>H<sub>8</sub> column uncertainties are generally  
 223 smaller than 10<sup>15</sup> molecules.cm<sup>-2</sup>. But since the columns themselves are even smaller, no C<sub>3</sub>H<sub>8</sub> is detected at  
 224 Barcroft. At the lower altitude sites such as JPL and Ft. Sumner, the increased interference from H<sub>2</sub>O and CH<sub>4</sub> cause  
 225 the C<sub>3</sub>H<sub>8</sub> column uncertainties to be much larger, generally around 5x10<sup>15</sup> molecules.cm<sup>-2</sup> at low airmass and  
 226 worsening rapidly toward higher airmasses. But the C<sub>3</sub>H<sub>8</sub> increases far more, allowing C<sub>3</sub>H<sub>8</sub> to be detected at these  
 227 low-altitude sites under polluted conditions, despite the poorer absolute uncertainties.

Deleted: This

Deleted: s

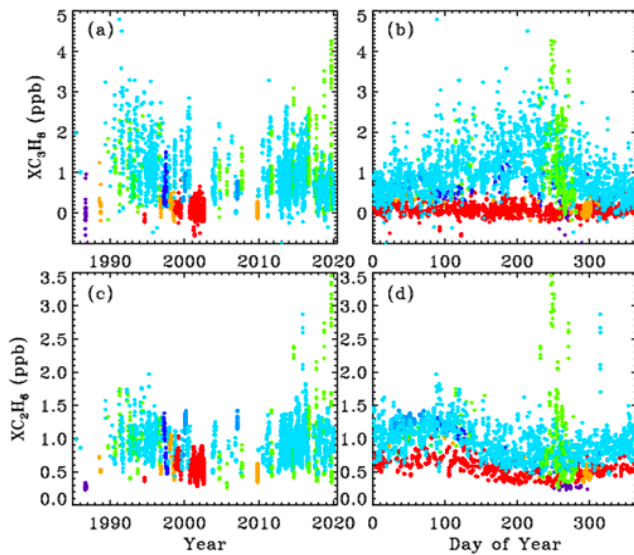
Formatted: Subscript

Formatted: Subscript

235 High  $C_3H_8$  values are also seen at Ft. Sumner, NM (lime), especially in recent years. This was initially a surprise to  
 236 us because this area has a very low population density, so we naively assumed that we would be measuring  
 237 background levels of atmospheric pollutants here.

238 We know that the apparent variations in  $C_3H_8$  are real, rather than artifacts, from their strong correlation with  $C_2H_6$ .  
 239 Figure 4 compares column-averaged  $C_3H_8$  mole fractions (top panels) with those of  $C_2H_6$  (bottom panels), the latter  
 240 retrieved using different spectral lines than those shown in Fig.2. These are the same total  $C_3H_8$  columns shown in  
 241 Fig.3, but divided by the total column of all gases, which is inferred from the surface pressure. The resulting  
 242 column-average mole fractions, denoted  $X_{gas}$ , are less sensitive to the site altitudes being different and more easily  
 243 compared with in situ measurements being in units of mole fraction.

244 The upper and lower rows of Fig.4 shows the  $X_{C_3H_8}$  and  $X_{C_2H_6}$  time series, respectively, plotted versus year (left)  
 245 and versus day of the year (right). The data were filtered such that only points with  $X_{C_3H_8}$  uncertainties  $< 0.74$  ppb  
 246 and  $C_2H_6$  uncertainties  $< 0.10$  ppb were plotted. This reduced the total number of points from 5000 to 4700, so only  
 247 the best 94% of the data are plotted. It is clear that at JPL (cyan)  $C_3H_8$  has decreased since the 1990s, but that at Ft.  
 248 Sumner (lime) it has increased over the past decade. The data from these two sites will be explored later.



249

250 **Figure 4.** Top panels show measurements of the column-averaged  $C_3H_8$  mole fractions ( $X_{C_3H_8}$ ). Bottom panels  
 251 show  $X_{C_2H_6}$ . Left panels show the variation with year. Right-hand panels show the seasonal variation. Points are  
 252 color-coded by observation site altitude as in Fig.3.

Deleted: c

Formatted: Font: Times New Roman, 10 pt

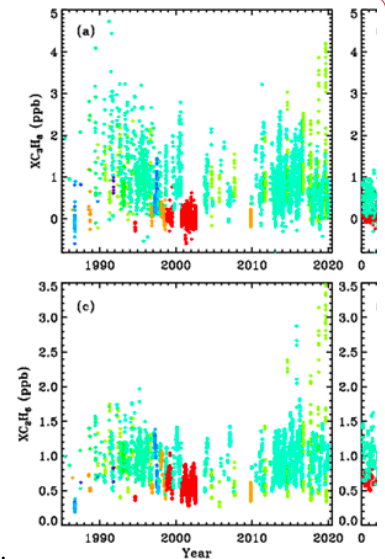
Formatted: Font: Times New Roman, 10 pt

Formatted: Font: Times New Roman, 10 pt

Formatted: Font: Times New Roman, 10 pt

Deleted: The left-hand panels of Fig.4 show the  $X_{C_3H_8}$  time series plotted versus year, and the right-hand panels versus day of the year.

Moved down [3]: The points are color-coded by observation site altitude using the same color scheme as in Fig.3.



Deleted:

Moved (insertion) [3]

Deleted: The p

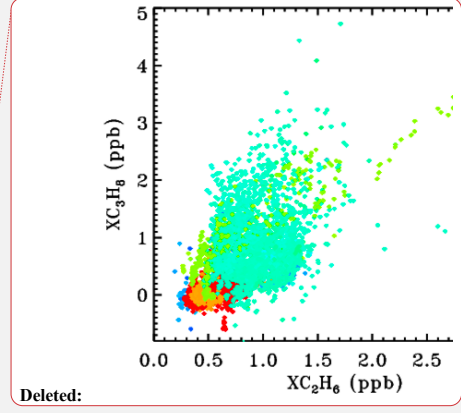
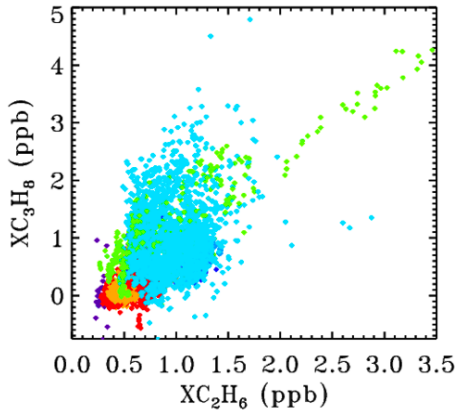
Deleted: using the same color scheme



262  $C_2H_6$  is four times longer-lived than  $C_3H_8$  and never goes to zero because there is always a substantial free  
 263 tropospheric  $C_2H_6$  component, even in the SH, which varies seasonally: high in spring, low in fall. The Antarctic  
 264 measurements (blue) are very low (0.2-0.3 ppb) and most probably even lower during the rest of the year, because  
 265 days 250 to 300 represent the springtime peak, not the fall. The highest  $C_2H_6$  ever measured from JPL (cyan) was in  
 266 late 2015 (day 314) as a result of the Aliso Canyon natural gas leak (Conley et al., 2016). This event is further  
 267 discussed later and also in Appendix C.

268 Figure 5 shows the  $XC_2H_6/C_3H_8$  correlation plot for all sites. This uses the exact same data, filtering, and color-  
 269 scheme as for Fig. 4. At JPL (cyan) the correlation is positive but weak. At Ft. Sumner, there are episodes of both  
 270 gases being enhanced with a strong correlation. In fact, the highest VMRs of  $C_2H_6$  were seen from Ft. Sumner, even  
 271 more than from JPL during the Aliso Canyon gas leak in late 2015.

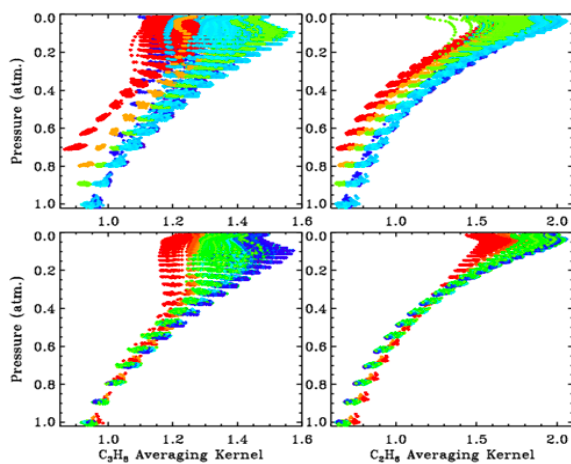
- Deleted: The lower panels of Fig.4 show  $XC_2H_6$ . Th
- Deleted: is
- Formatted: Subscript
- Formatted: Subscript
- Deleted: that
- Formatted: Font: Times New Roman, 10 pt
- Deleted: The Antarctic measurement (blue) are even lower than they appear because
- Deleted: in Antarctica
- Deleted: ever
- Deleted: was
- Deleted: there



272  
 273 **Figure 5.** The correlation between  $XC_2H_6$  and  $XC_3H_8$  for all sites, color-coded by site altitude as in Fig.3.

274 **3.1. Averaging Kernels.**

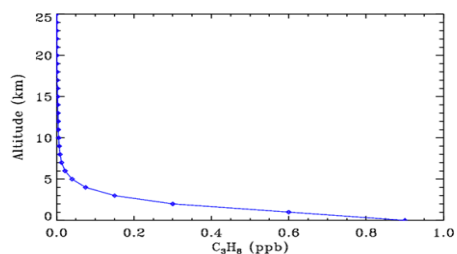
275 Figure 6 shows all kernels for the 5000 measurements presented in this paper, color-coded by site altitude (red=3.8  
 276 km; orange=2.2 km; lime=1.2 km; cyan=0.35 km; blue < 0.2 km) as in the main body of the paper. The kernels  
 277 increase with altitude but with <40% variation over the 0-30 km altitude range. Note that the kernels representing  
 278 the 3.8 km site begin at P=0.7 atm. And the kernels representing the 2.2 km site begin at P=0.8 atm.



289

290 *Figure 6: 5000 averaging kernels for Left: C<sub>3</sub>H<sub>8</sub> and Right: C<sub>2</sub>H<sub>6</sub>. Upper panel shows all kernels color-coded by*  
 291 *site altitude, as in Fig.3. Lower panel shows kernels for the low-altitude sites (0.25 to 0.50 km), which were all*  
 292 *colored blue in the upper panel, now color-coded by solar zenith angle (Blue=15°; Green=60°; Red=80°).*

293 *The lower panel shows the kernels for the low altitude sites (mainly JPL). These points were all cyan in the upper*  
 294 *panel but in the lower panel they are color-coded by Solar Zenith Angle. It is evident that the higher the SZA the*  
 295 *more uniform the kernels with altitude. The banding of the points in pressure space reflects the 1 km vertical grid on*  
 296 *which the kernels were computed. The C<sub>3</sub>H<sub>8</sub> kernels are also influenced by the H<sub>2</sub>O column and temperature, but*  
 297 *these are smaller effects than those of site altitude or SZA.*



298

299 *Figure 7. A priori C<sub>3</sub>H<sub>8</sub> profile used in these retrievals.*

300 Figure 7 show the assumed a priori vmr profile used in the retrievals and in the computation of the kernels. Since  
301 GFIT performs profile scaling retrievals, with a very weak a priori constraint, the absolute values of the vmrs play  
302 no role, only the profile shape matters.

Formatted: Space Before: 0 pt, After: 12 pt, Pattern: Clear

Formatted: Font: Not Bold

### 303 3.2. Case Study: Ground-based measurements from Ft. Sumner, NM

Deleted: 1

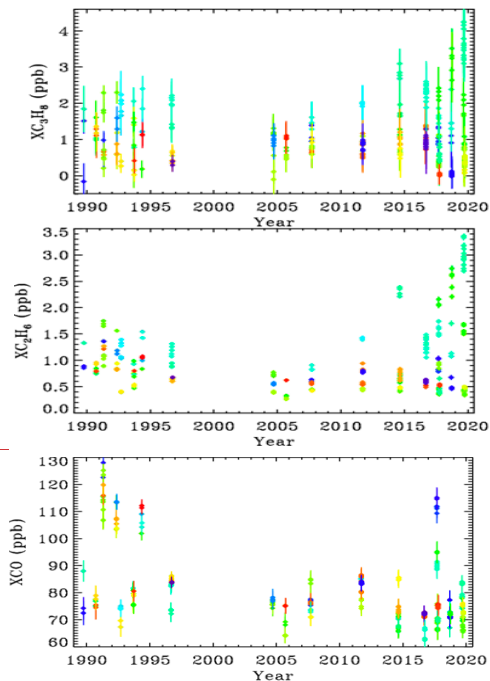
304 Ft. Sumner (34.48N, 104.22W, 1.2 km ASL) is the location of the main NASA facility for the launch of  
305 stratospheric research balloons. It is located here due to the low population density and hence low risk of mishap.  
306 The MkIV instrument has performed balloon campaigns in Ft. Sumner 18 times in the past 30 years. Not all of these  
307 campaigns have resulted in a flight, but we have always taken ground-based observations to check that the MkIV  
308 instrument is correctly aligned and functional, and to check that telemetry, commanding, and the operation of other  
309 experiments do not degrade the MkIV performance.

Deleted: . A

310 We have taken 520 observations on 106 different days from Ft. Sumner (out of a total of 5000 observations and  
311 1200 days). We examine these observations to try to understand whether the large day-to-day  $C_3H_8$  variations are  
312 real, and if so, what is causing them. We have already seen a correlation between the  $XC_3H_8$  and  $XC_2H_6$  at all sites  
313 in Fig.5, but many points are buried under others, especially at the low values of  $XC_3H_8$  and  $XC_2H_6$ .

Formatted: Indent: First line: 0", Space Before: Auto, After: Auto

Deleted: ¶



314

315

319 **Figure 8.**  $XC_3H_8$ ,  $XC_2H_6$  and  $XCO$  at Ft. Sumner. Since all the observations are made from the same altitude, it no  
320 longer makes sense to color code by site altitude. So instead we color-code by mean bearing of the back-trajectory  
321 over the previous 36 hours. Dark blue=30°; Light blue =90°; Cyan=120°; Green=180°; Lime=220°; Orange=  
322 300°; Red=350°. ~~MKIV didn't visit Ft. Sumner from 1997 to 2004 because it was performing high-latitude balloon~~  
323 ~~flights from Alaska and Sweden.~~

324

325 Figure 8 shows that between 1990 and 2005 there was a decrease in  $C_2H_6$  and  $C_3H_8$  measured in Ft. Sumner, by  
326 about a factor 2 over 15 years. In recent years (since 2014), however, there has been a large increase in  $C_2H_6$  and  
327  $C_3H_8$  measured at Ft. Sumner, but only when the wind direction is from the SE quadrant (green-cyan colors). We see  
328 no increase associated with other wind directions (red, blue, orange, yellow, lime).

329 At Ft. Sumner CO has no correlation with wind direction, nor with  $C_2H_6$  or  $C_3H_8$ . The majority of days have a  
330 column average CO of  $75 \pm 10$  ppb. But there are occasional enhancements up to 120 ppb, likely due to large but  
331 distant fires. We do not pursue the Ft. Sumner CO data any further, beyond proving that the  $C_3H_8$  sources are  
332 different from those of CO.

333  $CH_4$  is also measured by MkIV. Over the 30-year measurement period  $XCH_4$  has grown from 1650 to 1850 ppb.  
334 This secular increase is much larger than any variation due to wind direction. So to be useful, the  $CH_4$  data would  
335 have to be detrended, which is not simple given its non-linear growth. Even within the past 4 years, the correlation  
336 of  $XCH_4$  with  $XC_3H_8$  was very weak. This is to be expected since the background abundance of  $CH_4$  is more than  
337 1000x larger than  $C_3H_8$ , whereas wet NG is only 6 times richer in  $CH_4$  than  $C_3H_8$  (in the Permian basin). So the NG-  
338 induced enhancement of  $CH_4$ , as a fraction of its atmospheric background level, will be much smaller than that of  
339  $C_3H_8$ .

340 Figure 9 shows a  $XC_3H_8$ - $XC_2H_6$  scatter plot using just the Ft. Sumner data. Error bars are much larger for  $XC_3H_8$   
341 than for  $XC_2H_6$ . This is because the  $C_2H_6$  transitions are stronger and form narrower features, both of which make  
342 the retrievals more precise and definitive, whereas most of the  $C_3H_8$  absorption is smeared into a broad continuum  
343 which provides little information for a retrieval in which the continuum level is fitted. The  $C_2H_6$  features used in the  
344 actual  $C_2H_6$  retrieval are at 2976.6 and 2986.6  $cm^{-1}$  (not shown) and are 3–4 times stronger than those seen in Fig.2.

Moved down [5]: MKIV didn't visit Ft. Sumner from 1997 to 2004 because it was performing high-latitude balloon flights from Alaska and Sweden.

Deleted: 6

Moved (insertion) [5]

Deleted: .

Deleted: 6

Deleted: /lime

Deleted: . They are of no value

Deleted: other than

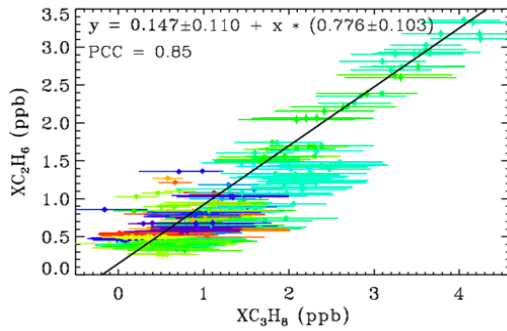
Deleted: from the Permian Basin

Deleted: .

Deleted: be more than 100 times

Deleted: 7

Deleted: this type of



359

360 **Figure 9.** The relationship between  $XC_3H_8$  and  $XC_2H_6$  at Ft. Sumner, color coded for wind direction as for Fig. 8.

361 The gradient of the fitted line is  $0.78 \pm 0.10$  implying more  $C_3H_8$  than  $C_2H_6$ . The Pearson Correlation coefficient is  
 362 0.85, which is high considering the large error bars on the  $XC_3H_8$ , and the fact that the similarity of their Jacobians  
 363 would imply an anti-correlation in their retrieved amounts (Appendix A). This tight relationship at Ft. Sumner  
 364 suggests that the large variations in the  $C_3H_8$  measurements are not an artifact. Since  $C_2H_6$  can be easily and  
 365 precisely measured by this technique, it is hard to imagine it being changed by a factor 5 from day to day by an  
 366 artifact. Much more likely, the common variations in both  $C_3H_8$  and  $C_2H_6$  are real.

367 As already hinted, for each of the 106 observation days from Ft. Sumner we ran hourly HYSPLIT back-trajectories  
 368 (Stein et al., 2015, Rolph et al., 2017) that bracket the MkIV observation times, then interpolated linearly in time  
 369 between the two bracketing trajectories. This provided a unique trajectory for each of the 520 observations from Ft.  
 370 Sumner. The North American Regional Reanalysis (NARR) meteorology was selected which covers North America  
 371 at 32 km resolution. This is the highest resolution meteorology that covers the entire 1989–2019 observation period.  
 372 A trajectory altitude of 0.4 km over Ft. Sumner was selected, and these trajectories were extended to 36 hours before  
 373 the observations in 1-hour steps. Fig. 10 shows that the large variations of  $C_3H_8$  are strongly correlated with wind  
 374 direction. It is very clear that trajectories originating to the SE of Ft. Sumner, carry more  $C_3H_8$  than those from any  
 375 other direction. A plot was made also for  $C_2H_6$  but not shown due to its strong similarity to Fig. 10.

Deleted: 7

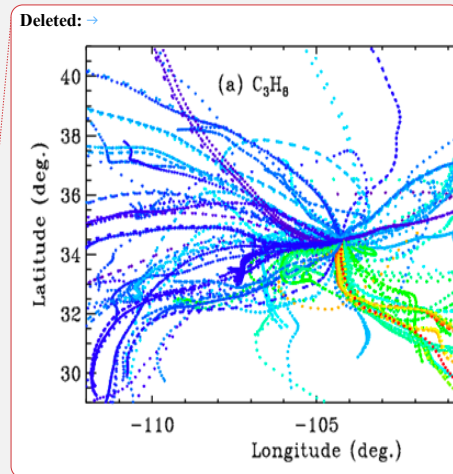
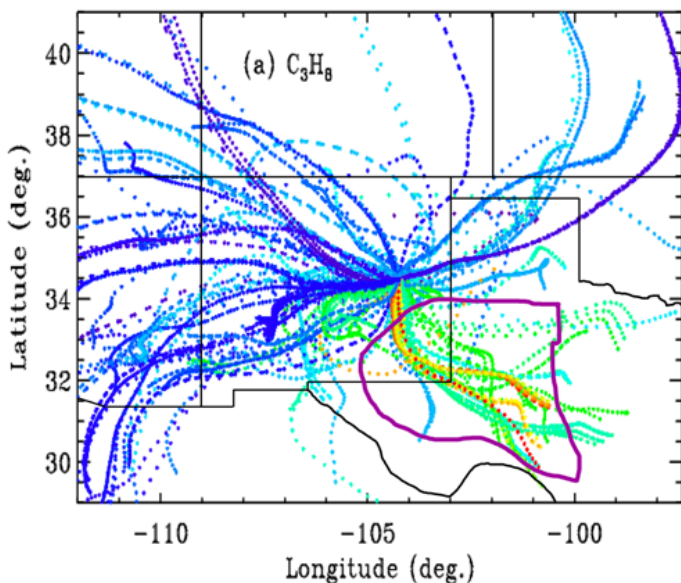
Deleted: 6

Deleted: .

Deleted: implic

Deleted: 8

Deleted: 8



382

383 **Figure 10.** Hourly locations for the back-trajectories, color-coded by retrieved  $XC_3H_8$ . Blue=0 ppb, Green=2 ppb;  
 384 Red=4 ppb. Trajectories for which the  $XC_3H_8$  uncertainty exceeded 0.74 ppb are excluded, resulting in only 373 out  
 385 of 520 trajectories being shown. Ft. Sumner lies at 34.2N, 104.2W, close to the center of the figure at the confluence  
 386 of all the back-trajectories. Each point represents a 1-hour time step, so that the wind speed is apparent from the  
 387 separation of points. Winds from the West are typically stronger than those from the SE quadrant. Trajectories are  
 388 underlaid by a map of New Mexico and neighboring states. The Permian Basin, encircled by the thick purple line,  
 389 underlies SE New Mexico and much of West Texas. Many of the trajectories from the SE have spent 30+ hours over  
 390 the Permian Basin.

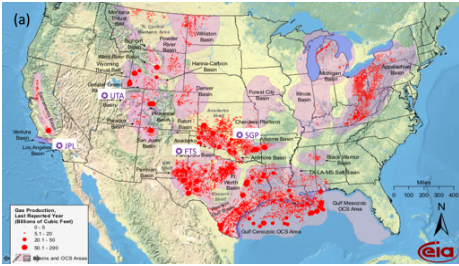
Deleted: 8  
 Deleted: .  
 Deleted:  
 Deleted: nd

391 We also made a scatter plot for CO (not shown) but there was no correlation between CO and wind direction, or  
 392 between CO and  $C_3H_8$ . This rules out the possibility that the enhanced  $C_3H_8$  and  $C_2H_6$  were somehow associated  
 393 with distant urban pollution or wild fires.

394 This result leads to speculation on what might be enhancing  $C_2H_6$  and  $C_3H_8$  when the winds come from the SE  
 395 sector. One of the biggest natural gas production fields in the US lies in the Permian Basin, which underlies the  
 396 South-East corner of New Mexico and West Texas, as illustrated in Figure 10. This region also includes processing  
 397 plants where the heavier gases are stripped out of the wet NG, storage facilities for the resulting Natural Gas Liquids  
 398 (LPG+ethane+pentane), and pipelines. The Permian Basin is by far the largest "liquids-rich" (rich in heavy  
 399 hydrocarbons) gas field in the USA ([https://www.spglobal.com/platts/plattscontent/\\_assets/\\_images/latest-](https://www.spglobal.com/platts/plattscontent/_assets/_images/latest-)

Deleted: 9

407 [news/20191219-rig-count.jpg](#)). This would suggest that the enhanced C<sub>2</sub>H<sub>6</sub> and C<sub>3</sub>H<sub>8</sub> is the result of losses from NG  
 408 production, although this cannot be proven with just one instrument at one site. We would need instruments upwind  
 409 and downwind to make an accurate assessment of the fluxes.



410  
 411  
 412 **Figure 11.** NG production in the lower 48 states of the USA in 2009. Data from the Energy Information  
 413 Administration: [https://www.eia.gov/oil\\_gas/rpd/conventional\\_gas.pdf](https://www.eia.gov/oil_gas/rpd/conventional_gas.pdf). Superimposed are the locations (purple  
 414 pentangular star) of the four sites discussed in detail in this paper: Ft. Sumner in Eastern NM is labelled "FTS". The  
 415 JPL site in California is labelled "JPL". The locations of the NOAA sites in Utah (UTA) and Oklahoma (SGP) are  
 416 also included. The Permian basin lies in the SE corner of NM and West Texas.

417 The Permian basin currently produces 16 billion cu.ft./day of NG  
 418 (<https://www.eia.gov/petroleum/drilling/pdf/permian.pdf>) over an area of 220,000 km<sup>2</sup>. The molar volume of an  
 419 ideal gas at STP is 22.4 liters. One cu. ft. is 28.3 liters. So 16 billion cu. ft. is 20 billion moles of NG or 120x10<sup>32</sup>  
 420 molecules per day. Over an area of 220,000 km<sup>2</sup> or 2.2x10<sup>15</sup> cm<sup>2</sup>, this represents an average areal production of  
 421 55x10<sup>17</sup> molec./cm<sup>2</sup>/day. Assuming that the Permian basin is 480 km wide, at an average low-level wind speed of 15  
 422 km/hour, an air parcel will take 32 hours (1.33 days) to traverse the Basin, during which time 73x10<sup>17</sup>  
 423 molecules/cm<sup>2</sup> will have been extracted. Of this, 10% will be C<sub>3</sub>H<sub>8</sub> (Howard et al., 2015), so if all this production  
 424 were released into the atmosphere we would expect a C<sub>3</sub>H<sub>8</sub> column enhancement of 73x10<sup>16</sup>.

425 In airmasses with trajectories from the SE, we see maximum C<sub>3</sub>H<sub>8</sub> column enhancements of only 3x10<sup>16</sup>  
 426 molecules/cm<sup>2</sup>, which suggests that only 4% of the NG escapes into the atmosphere and that 96% of the NG is  
 427 successfully captured (or burnt by flaring).

428 In the Permian Basin, NG is 13.7% C<sub>2</sub>H<sub>6</sub> and yet the observed ethane enhancements are slightly smaller than those  
 429 of C<sub>3</sub>H<sub>8</sub>, suggesting that only ~3% of the NG escapes. Assuming a 3% leak rate, there will also be an enhancement  
 430 of CH<sub>4</sub> of about 14x10<sup>16</sup> molec.cm<sup>-2</sup>, but this represents only 0.4% of the total CH<sub>4</sub> column above Ft. Sumner and  
 431 will therefore be difficult to discern in the presence of other confounding factors (stratospheric transport, varying  
 432 tropopause altitude, seasonal and longer-term changes). Of course, all this analysis assumes that the Permian basin

- Deleted: 9
- Deleted: (a)
- Deleted: (b): [Temporarily removed -- awaiting permission] Illustrating the high number of "liquids-rich" drilling rigs in the Permian Basin, as of Dec. 2019, underscoring its dominance for propane production in the USA. From <https://www.spglobal.com/platts/en/market-insights/latest-news/natural-gas/121919-us-oil-gas-rig-count-rises-for-second-straight-week-everus>
- Formatted: Font: Times New Roman, 10 pt
- Formatted: Line spacing: 1.5 lines
- Formatted: Font: Times New Roman, 10 pt
- Formatted: Font: Times New Roman, 10 pt
- Formatted: Font: 10 pt
- Deleted: In recent years, the Permian basin has been producing ~15 billion cu.ft. of natural gas (NG) per day (<https://www.eia.gov/petroleum/drilling/pdf/permian.pdf>). A back-of-the-envelope estimate of the contribution of this to the observed C<sub>3</sub>H<sub>8</sub> is now performed. We assume that this NG production is distributed over an area that is 160 km across. At a wind speed of 20 km/hour, an airmass will take 8 hours to traverse the gas field, during which time 0.72E+19 molecules.cm<sup>-2</sup> of NG will have been extracted. Howard et al., (2015), measured the composition of NG from the Permian basin and found that it is very rich in heavy hydrocarbons, being 66.6% CH<sub>4</sub>, 13.7% C<sub>2</sub>H<sub>6</sub> and 10.3% C<sub>3</sub>H<sub>8</sub> by volume. If 4% of this were lost to the atmosphere, and 10.3% of this is C<sub>3</sub>H<sub>8</sub>, the total propane column will be enhanced by 3E+16 molecules.cm<sup>-2</sup>, which is close to that seen in the highest cases. For
- Deleted: C<sub>2</sub>H<sub>6</sub>,
- Formatted: Subscript
- Formatted: Subscript
- Deleted: an
- Deleted: of 4E+16
- Deleted:
- Deleted: would be expected for such a back-trajectory, which is somewhat higher than measured
- Deleted: T
- Deleted: 9E+
- Deleted: 5

468 is a uniform emitter and that the back trajectory wind speeds are accurate. There are likely hot spots with higher-  
469 than-average emissions, and regions with little NG production.

470 A puzzle in our findings is that when both C<sub>3</sub>H<sub>8</sub> and C<sub>2</sub>H<sub>6</sub> are elevated, we measure 22% more C<sub>3</sub>H<sub>8</sub> than C<sub>2</sub>H<sub>6</sub> (see  
471 fig.9). Yet independent essays of well-head wet NG find 33% more C<sub>2</sub>H<sub>6</sub> than C<sub>3</sub>H<sub>8</sub> in the Permian basin (Howard et  
472 al., 2015). So we have a 55% discrepancy. We note that the C<sub>2</sub>H<sub>6</sub> averaging kernel is 0.7 at the surface versus 0.9 for  
473 C<sub>3</sub>H<sub>8</sub> (see Appendix B). So when these gases exceed their priors in the PBL, which is likely at high enhancements,  
474 both will be under-estimated, but C<sub>2</sub>H<sub>6</sub> more so than C<sub>3</sub>H<sub>8</sub>. So this effect would cause the C<sub>3</sub>H<sub>8</sub>/C<sub>2</sub>H<sub>6</sub> ratio to be 28%  
475 high, which explains half the 55% problem. Another possibility is that the C<sub>3</sub>H<sub>8</sub> coming from fugitive wet NG is  
476 augmented by leaks of LPG, stripped from wet NG. This would further enhance the C<sub>3</sub>H<sub>8</sub> (and C<sub>4</sub>H<sub>10</sub>) with little  
477 C<sub>2</sub>H<sub>6</sub> increase. Alternatively, there could be a systematic over-estimate of the MkIV C<sub>3</sub>H<sub>8</sub> due to a mundane  
478 multiplicative bias in the C<sub>3</sub>H<sub>8</sub> spectroscopy. This would over-estimate all the C<sub>3</sub>H<sub>8</sub> measurements without  
479 degrading the strong correlation with C<sub>2</sub>H<sub>6</sub>, but seems unlikely.

### 480 3.3 Case Study: Ground-based measurements from JPL

481 The Jet Propulsion Laboratory (34.2N; 118.17W; 0.35 km altitude) lies at the Northern edge of the Los Angeles  
482 basin. When winds are from the North (rare in summer) air quality is good. When conditions are stagnant (common  
483 in summer) pollutants accumulate and so air quality is poor. C<sub>3</sub>H<sub>8</sub> measured at JPL exhibits very different behavior  
484 to that at Ft. Sumner. It decreases over time, exhibits little correlation with C<sub>2</sub>H<sub>6</sub>, and positive correlation with CO.  
485 Figure 12 illustrates these behaviors.

486 The left-hand panels of Fig. 12 shows XC<sub>3</sub>H<sub>8</sub> time series measured from JPL, color coded by CO. The upper-left  
487 panel shows a large decrease in C<sub>3</sub>H<sub>8</sub> from 1–3 ppb in 1990 to less than 1 ppb in 2019. This mirrors the decrease in  
488 CO over JPL (not shown) over the same period. The lower-left panel shows a large seasonal component to the  
489 C<sub>3</sub>H<sub>8</sub>, with a peak in late summer, when the air is most stagnant over JPL allowing pollutants to accumulate. The  
490 highest C<sub>3</sub>H<sub>8</sub> values appear red or orange (high CO), while the lowest appear blue (low CO), implying an  
491 association with CO. This is confirmed in the upper-right panel which plots C<sub>3</sub>H<sub>8</sub> directly against CO. The right-  
492 hand panels are color-coded by year. The C<sub>3</sub>H<sub>8</sub> correlation is mostly a result of both gases having decreased over the  
493 30-year record. But even within each year, there still remains a positive correlation. This does not necessarily mean  
494 that C<sub>3</sub>H<sub>8</sub> and CO have the same source, but that their sources are spatially coincident.

Deleted: Of course, in cases of higher wind-speeds, or trajectories that partially circumvent the basin, the duration will be less than 8 hours and so the uptake of hydrocarbons will be smaller. ¶

Deleted: .

Deleted: always

Moved down [4]: One possibility is that the C<sub>3</sub>H<sub>8</sub> coming from leaking wet NG is augmented by leaks of LPG, stripped from wet NG. This would further enhance the C<sub>3</sub>H<sub>8</sub> (and C<sub>4</sub>H<sub>10</sub>) with little C<sub>2</sub>H<sub>6</sub> increase.

Deleted: ¶

Formatted: Not Superscript/ Subscript

Deleted: /C<sub>3</sub>H<sub>8</sub>

Deleted: 5

Deleted: low

Deleted:

Deleted: m, but not all

Moved (insertion) [4]

Deleted: One

Deleted: leaking

Deleted: ¶

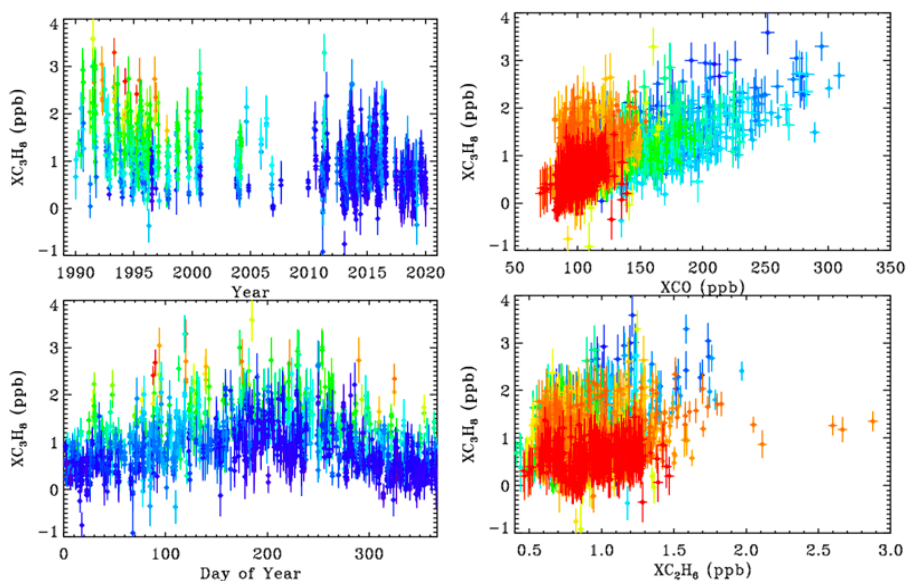
¶

Deleted: 2

Deleted: 0

Deleted: 0





518

519 **Figure 12.** Column-average  $C_3H_8$ s above JPL. **Left Panels:** The time series color-coded by CO (red=250 ppb;  
 520 green= 130 ppb; blue=100 ppb). **Right Panels:** The relationship between  $XC_3H_8$ s and CO and  $C_2H_6$  color-coded by  
 521 year (blue=1990; green=2005; red=2019).

522

523 The lower-right panel shows  $C_3H_8$  plotted versus  $C_2H_6$ . There is a weak correlation at JPL. The high  $XC_2H_6$  values  
 524 exceeding 2.0 ppb were measured in day 314 of 2015 when JPL was downwind of the Aliso Canyon NG leak.

525 Appendix C shows a HYSPLIT back-trajectory confirming this assertion. This spike can also be seen in Fig. 3.

526 There is no  $C_3H_8$  enhancement associated with the  $C_2H_6$  spike, since processed NG was leaking from an  
 527 underground storage facility, the heavy hydrocarbons (e.g.,  $C_3H_8$ ,  $C_4H_{10}$ ) having already been stripped out. A 2%  
 528 increase in column-averaged  $CH_4$  was also noted in the plume of the Aliso Canyon leak, as shown in Appendix C.

529 California accounts for less than 1% of total U.S. natural gas production and this has declined over the past three  
 530 decades (<https://www.eia.gov/state/analysis.php?sid=CA>). Although there is natural gas extraction in the LA basin,  
 531 this is a small source compared with the Permian basin. The local natural gas is only 3%  $C_2H_6$  and 0.3%  $C_3H_8$ ,  
 532 (<https://www.socalgas.com/stay-safe/pipeline-and-storage-safety/playa-del-rey-storage-operations>) and so cannot  
 533 account for the approximately equal amounts of these gases measured at JPL by the MkIV. We speculate that the  
 534  $C_3H_8$  measured at JPL comes mainly from LPG (e.g., used in "clean" commercial vehicles, BBQ grills, external  
 535 heaters, etc.). We can certainly rule out the possibility that the  $C_3H_8$  measured at JPL is the result of wild fires, since  
 536 these have increased in recent years whereas the  $C_3H_8$  has decreased.

Deleted: 0

538 **3.4 Comparison with In Situ Measurements**

539 **First it should be pointed out that** the column-average mole fractions that are derived from the column measurements  
540 will under-estimate the gas amount in the PBL for gases like C<sub>2</sub>H<sub>6</sub> and C<sub>3</sub>H<sub>8</sub> that reside mainly in the PBL. For  
541 example, if C<sub>3</sub>H<sub>8</sub> resides entirely between 1000 and 800 mbar, with none in the free troposphere or stratosphere,  
542 then the column-average values will be 5 times smaller than the actual mole fractions in the PBL. So direct  
543 comparisons of the remote and in situ mole fractions should be avoided. But their behavior as a function of year or  
544 season, or gas-to-gas correlations, can still be meaningfully compared. This effect is in addition to the effect of their  
545 averaging kernels being less than 1.0 at the surface, which was discussed earlier.

546 In situ C<sub>3</sub>H<sub>8</sub> and C<sub>2</sub>H<sub>6</sub> mole fractions from the Wendover, Utah (UTA) and Southern Great Plains, Oklahoma (SGP)  
547 sites were downloaded from the NOAA Global Monitoring Laboratory website:  
548 (<https://www.esrl.noaa.gov/gmd/dv/data/>). These sites are the closest to Ft. Sumner. These are surface flask  
549 measurements covering the period 2006 to 2017. Figure 13 illustrates these data as a function of the year (left  
550 panels), the day of the year (middle panels), and the C<sub>3</sub>H<sub>8</sub>-C<sub>2</sub>H<sub>6</sub> relationship (right panels). The upper panels cover  
551 the UTA site and the lower panels the SGP site. Note the factor 10 change in the y-scale: there is 10x more of these  
552 gases at SGP than at UTA. Looking at the map in Fig. 11, this is clearly because SGP lies immediately downwind of  
553 the Anadarko Basin oil and NG fields under the prevailing WSW winds. In contrast, the UTA site has no major up-  
554 wind source.

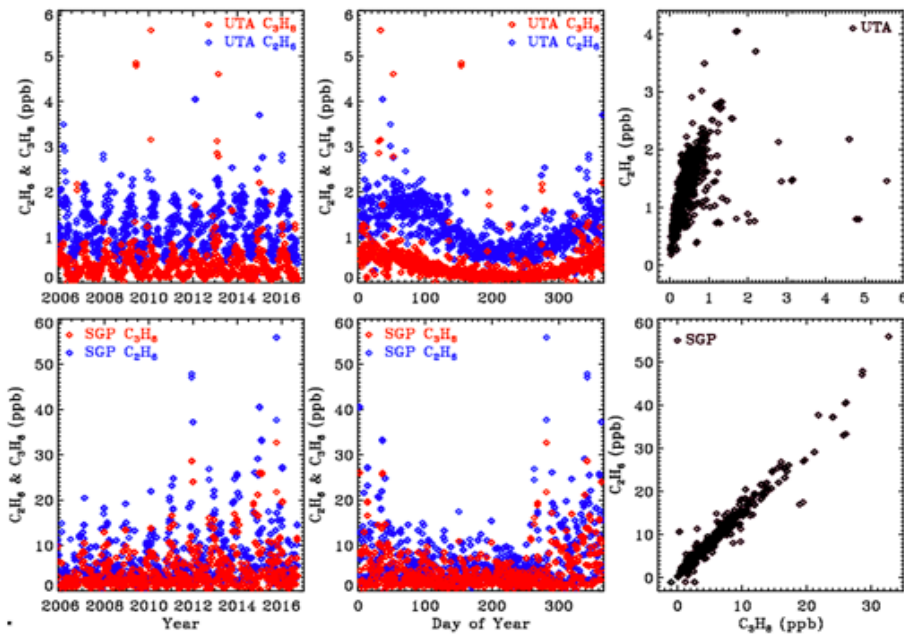
555 These in situ measurements confirm that C<sub>3</sub>H<sub>8</sub> is highly variable with large enhancements being associated with oil  
556 and NG production fields. At SGP the C<sub>3</sub>H<sub>8</sub>/C<sub>2</sub>H<sub>6</sub> ratio is about 0.65. This is smaller than those measured by the  
557 MkIV, but NG in the Permian basin is much wetter (richer in C<sub>3</sub>H<sub>8</sub>) than in the Anadarko basin.

Deleted: 3

Deleted: First a caveat:

Deleted: 1

Deleted: 9



562

563 **Figure 13.** In situ flask measurements of  $C_3H_8$  (red) and  $C_2H_6$  (blue) from the NOAA ESRL GMD dataset (Helmig  
 564 et al., 2017). Top panels show results from the UTA site and lower panels from SGP. Note the factor 10 change in  
 565 the y-scale between the two sites. Left panels plot data versus year to illustrate secular trends. Middle panels versus  
 566 Day of year to more clearly see the seasonal cycle. Right panels plot  $C_3H_8$  versus  $C_2H_6$ .

567

568 **3.5. Balloon Results**

569 We also attempted to retrieve  $C_3H_8$  from MkIV balloon solar occultation spectra. It was not detected in any flight,  
 570 despite a very good sensitivity of 0.05 ppb above 5 km. This confirms that the  $C_3H_8$  detected in ground-based  
 571 measurements, reaching column average mole fractions of up to 4 ppb, resides mostly in the PBL. The balloon  
 572 launches are typically performed only under stable, quiescent, meteorological conditions with light surface winds.  
 573 Such conditions preclude uplift of air from the PBL into the free troposphere, so that  $C_3H_8$  stays confined to the  
 574 PBL, which is opaque in limb paths due to aerosol, and so cannot be probed in occultation. This does not preclude  
 575  $C_3H_8$  getting up into the free troposphere at other times or in other places.

576

577

Deleted: 1

Deleted: 4

580 **4. Summary and Conclusions**

581 We report measurements of atmospheric C<sub>3</sub>H<sub>8</sub> by solar absorption spectrometry in the strong Q-branch region at  
582 2957 cm<sup>-1</sup>, using high resolution IR spectra from the JPL MkIV interferometer. To the best of our knowledge, these  
583 are the first remote sensing measurements of atmospheric C<sub>3</sub>H<sub>8</sub>. The minimum detectable abundance is about 10<sup>16</sup>  
584 molecules.cm<sup>-2</sup>, which is roughly equivalent to a column average mole fraction of 0.5 ppb. This allows C<sub>3</sub>H<sub>8</sub> to be  
585 measured in locations where its abundance is enhanced by proximity to sources (e.g., large gas fields, mega-cities),  
586 but not in clean locations (e.g. above the PBL or away from sources). We encourage such NDACC and TCCON  
587 sites to examine their datasets for C<sub>3</sub>H<sub>8</sub>. Future improvements to the spectroscopy of the interfering gases, e.g. H<sub>2</sub>O,  
588 CH<sub>4</sub>, C<sub>2</sub>H<sub>6</sub>, and other CH-containing gases currently missing might even provide for the detection of C<sub>3</sub>H<sub>8</sub> from  
589 clean sites at background levels, allowing it to become a routine product of the NDACC and TCCON networks.

- Formatted: Subscript
- Formatted: Subscript
- Deleted: e
- Deleted: a

590 A case study of ground-based MkIV measurements from Ft. Sumner, New Mexico, shows increasing C<sub>3</sub>H<sub>8</sub> and C<sub>2</sub>H<sub>6</sub>  
591 amounts in the past decade on days when back-trajectories came from SE New Mexico and West Texas, where the  
592 Permian Basin oil and gas field is located. A case study of C<sub>3</sub>H<sub>8</sub> measured at JPL shows a long-term decrease since  
593 1990 by more than a factor 2. It also shows a strong correlation with CO, a tracer of urban pollution. There is no  
594 significant correlation between C<sub>3</sub>H<sub>8</sub> and C<sub>2</sub>H<sub>6</sub> at JPL.

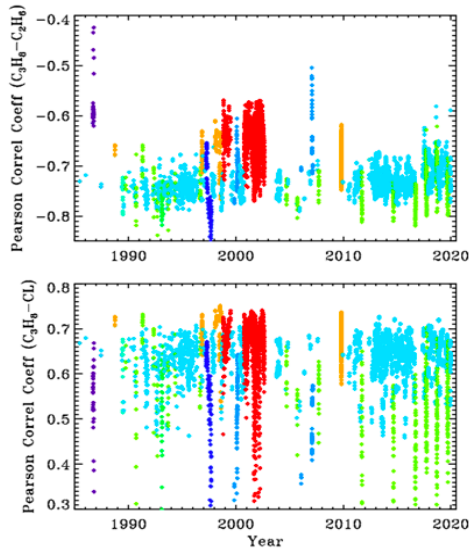
595 The MKIV measurements in the case studies are not particularly useful for determining the long-term global trends  
596 in C<sub>3</sub>H<sub>8</sub> or C<sub>2</sub>H<sub>6</sub>, due to their close proximity to strong sources. In the case of the Ft. Sumner the source is the  
597 Permian Basin. In the case of JPL the source is the Los Angeles urban area with a population of ~15M. These  
598 sources cause large meteorology-driven fluctuations that mask the longer-term trends.

599 From balloon measurements in solar occultation, propane was analyzed using the same window as for the ground-  
600 based measurements. It was not detected at any altitude in any of our 25 flights, despite a 0.05 ppb detection limit.  
601 This is presumably because under the stable atmospheric conditions that allow balloon launches, C<sub>3</sub>H<sub>8</sub> stays  
602 confined to the PBL, which is opaque in the limb viewing geometry and so cannot be probed.

603 **Appendix A: Correlations between retrieved parameters**

604 We compute Pearson Correlation Coefficients (PCC) from the a posteriori covariance matrix for each of the 5000  
605 spectral fits. The figures on the upper-left show the PCC between retrieved C<sub>3</sub>H<sub>8</sub> and C<sub>2</sub>H<sub>6</sub>. Points are plotted versus  
606 year with the same site-altitude-dependent coloring as in the other figures. The PCC between C<sub>3</sub>H<sub>8</sub> and C<sub>2</sub>H<sub>6</sub>  
607 averages about -0.7, which means that they are fairly strongly anti-correlated. This is due to their overlapping  
608 absorption features at 2967.5 cm<sup>-1</sup>. So as retrieved C<sub>2</sub>H<sub>6</sub> increases, retrieved C<sub>3</sub>H<sub>8</sub> will decrease, and vice versa. The  
609 PCCs are closer to zero for the high-altitude sites (red & orange), presumably due to the reduced pressure  
610 broadening and H<sub>2</sub>O causing the C<sub>2</sub>H<sub>2</sub> and C<sub>2</sub>H<sub>6</sub> absorption features to become more distinct. This anti-correlation  
611 could be reduced by use of a wider window to introduce additional C<sub>2</sub>H<sub>6</sub> features that don't correlate with C<sub>3</sub>H<sub>8</sub>, but  
612 this would also encompass large residuals without adding any C<sub>3</sub>H<sub>8</sub> information.

- Formatted: Font: Times New Roman, Not Italic, Font color: Text 1
- Formatted: Line spacing: 1.5 lines
- Formatted: Font: Times New Roman, Not Italic, Font color: Text 1
- Formatted: Subscript
- Formatted: Font: Times New Roman, Not Italic, Font color: Text 1
- Formatted: Font: Times New Roman, Not Italic, Font color: Text 1
- Deleted: overlap the
- Deleted: Q-branch



617

618 **Figure A.1.** Pearson Correlation Coefficients between  $C_3H_8$  and  $C_2H_6$  (upper panel) and between  $C_3H_8$   
 619 and the continuum level (CL) (lower panel)

620 The  $C_3H_8$ -CL correlations are about +0.65 at low SZA, decreasing at higher SZA as the  $H_2O$  and  $CH_4$  absorptions  
 621 black out the window. So the more  $C_3H_8$  that is retrieved, the higher the continuum level has to be to match the  
 622 measured spectrum, due to the fact that the  $C_3H_8$  absorption spectrum has a broad continuum-like component  
 623 beneath the Q-branch. The PCCs between  $C_3H_8$  and the other retrieved parameters (e.g.  $H_2O$ , HDO,  $CH_4$ ,  
 624 Continuum Tilt, Frequency Shifts) were all much closer to zero than with  $C_2H_6$  and CL.

625 The high PCC between  $C_3H_8$  and  $C_2H_6$  doesn't necessarily imply a large uncertainty in the  $C_3H_8$ . It just means that  
 626 the large component of the  $C_2H_6$  uncertainty gets projected onto the  $C_3H_8$ . Ditto for the CL. But provided the  $C_2H_6$   
 627 and CL are well retrieved, their effect on the  $C_3H_8$  will not dominate.

628

#### 629 Appendix B: Sensitivity of retrieved $C_3H_8$ columns to assumed P, T, and $H_2O$ profiles.

630

631 The retrievals shown in the main body of the paper were performed using 6-hourly NCEP analyses of T, P, and  $H_2O$ ,  
 632 as used in the GGG/TCOON analyses (Wunch et al., 2011). Due to the overlap of strong  $H_2O$  and  $CH_4$  lines with the  
 633  $C_3H_8$  Q-branch, we were concerned that small errors in the assumed T/P/ $H_2O$ / $CH_4$  priors might strongly influence  
 634 the retrieved  $C_3H_8$ . We therefore re-retrieved  $C_3H_8$  over the 2000–2020 period using the GEOS-FP-IT 3-hourly

Formatted: Font: Bold, Font color: Text 1

Formatted: Line spacing: 1.5 lines

Formatted: Font color: Text 1

Formatted: Font color: Text 1, Subscript

Formatted: Font color: Text 1

Formatted: Font color: Text 1, Subscript

Formatted: Font color: Text 1, Subscript

Formatted: Font color: Text 1

Formatted: Font color: Text 1

Formatted: Font color: Text 1, Subscript

Formatted: Font color: Text 1

Formatted: Font color: Text 1, Subscript

Formatted: Font color: Text 1

Formatted: Font color: Text 1, Subscript

Formatted: Font color: Text 1

Formatted: Font: Times New Roman, 10 pt, Not Italic, Font color: Text 1

Formatted: Space After: 6 pt, Line spacing: 1.5 lines

Formatted: Font: 10 pt, Not Italic, Font color: Text 1

Formatted: Font: 10 pt, Not Italic, Font color: Text 1, Subscript

Formatted: Font: 10 pt, Not Italic, Font color: Text 1

Formatted: Font: 10 pt, Not Italic, Font color: Text 1, Subscript

Formatted: Font: 10 pt, Not Italic, Font color: Text 1

Formatted: Font: Times New Roman, 10 pt, Not Italic, Font color: Text 1

Formatted: Font: 10 pt, Not Italic, Font color: Text 1

Formatted: Font: Times New Roman, 10 pt, Not Italic, Font color: Text 1

Formatted: Font: 10 pt, Not Italic, Font color: Text 1

Formatted: Font: Times New Roman, 10 pt, Not Italic, Font color: Text 1

Formatted: Font color: Text 1

Deleted: A

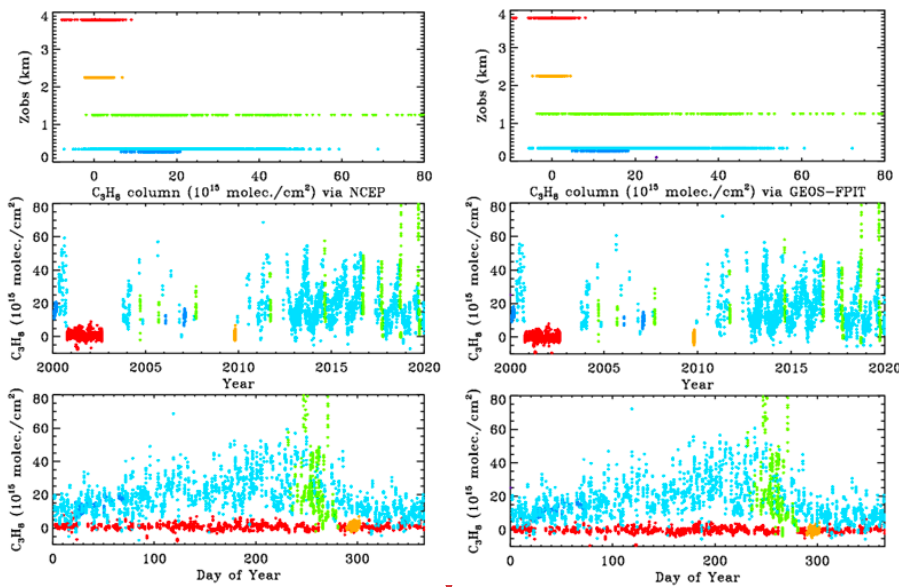
Deleted: exactly

Deleted: 2014

Deleted: 06

639 analyses, which forms the basis of the latest (GGG2020) TCCON analysis (Laughner et al., 2021). We would have  
 640 done the entire analysis with the GEOS-FP-IT model, except that it only supports the post-2000 time period.

641 Figure B.1 compares the retrieved  $C_3H_8$  columns from the two analysis methods: NCEP in the left panels and  
 642 GEOS-FP-IT in the right-hand panels. The results look very similar.

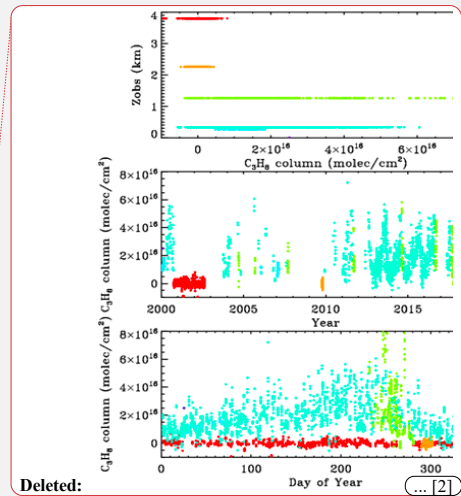


643  
 644 **Figure B.1.** Retrieved vertical columns of  $C_3H_8$  from 2000 to 2020 using two different atmospheric models. Left:  
 645 NCEP a priori T/P/H<sub>2</sub>O. Right: GEOS-FPIT a priori T/P/H<sub>2</sub>O. Points are color-coded by site altitude, as in Fig. 3.

646 Figure B.2 examines more closely the  $C_3H_8$  columns from the two analyses. In the upper panel the NCEP and  
 647 GEOS-FPIT columns are plotted against each other. The gradient is  $1.011 \pm 0.003$  with NCEP producing slightly  
 648 larger columns. The Pearson correlation coefficient is +0.979. The column differences, shown in the lower panel,  
 649 are mostly less than  $5 \times 10^{15}$  and are centered around zero at all column amounts. So the choice of models and priors  
 650 makes surprisingly little difference to the retrieved  $C_3H_8$ . This does not mean that the  $C_3H_8$  is highly accurate. There  
 651 are many things that are identical between the two analysis (e.g., spectroscopy, retrieval code, spectra) which could

Deleted: 0

Deleted: A



Deleted: ... [2]

Deleted: A

Deleted: Vertical columns of  $C_3H_8$  retrieved using the

Deleted: Vertical columns of  $C_3H_8$  retrieved using the

Deleted: -

Formatted: Indent: Left: 0", First line: 0"

Deleted: A

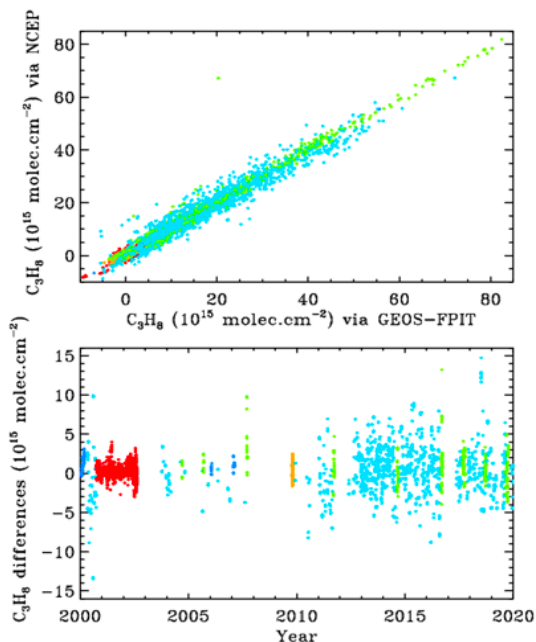
Deleted: 0.

Deleted: E<sup>+</sup>

Deleted: 6

Deleted:

666 nevertheless contribute large errors to the retrieved C<sub>3</sub>H<sub>8</sub>.

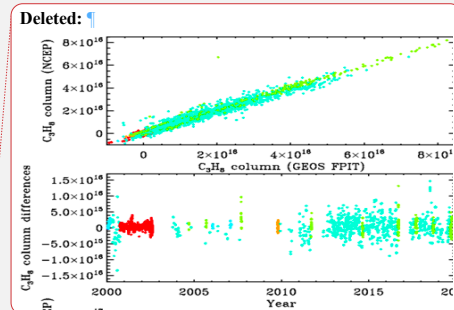


667

668 **Figure B.2.** Comparing the C<sub>3</sub>H<sub>8</sub> columns retrieved from the 6-hourly NCEP and the 3-hourly GEOS-FPIT priors,  
669 color-coded by site altitude. In the upper panel the columns are plotted against each other. In the lower panel their  
670 difference is plotted.

671 **Appendix C: - Aliso Canyon Underground Storage Facility: Gas Leak in late 2015**

672 Aliso Canyon Underground Storage Facility is located 30 km NW of JPL. According to the Jan 4, 2016,  
673 Los Angeles Times, NG leak began Oct 23, 2015 and peaked on Nov 28 at 60 Tons of CH<sub>4</sub> per hour. By Dec 22 leak  
674 rate had decreased to 30 Tons per hour as the underground storage pressure dropped from the initial 2700 psi.



Deleted: A

Deleted: F

Deleted: Appendix B: C<sub>3</sub>H<sub>8</sub> and C<sub>2</sub>H<sub>6</sub> Averaging kernels  
Figure B.1 shows all kernels for the 5000 measurements presented in this paper, color-coded by site altitude (red=3.8 km; orange=2.2 km; lime=1.2 km; cyan=0.35 km; blue < 0.2 km) as in the main body of the paper. The kernels increase with altitude but with <40% variation over the 0-30 km altitude range. Note that the kernels representing the 3.8 km site begin at P=0.7 atm. And the kernels representing the 2.2 km site begin at P=0.8 atm. [31]

Deleted: C



713

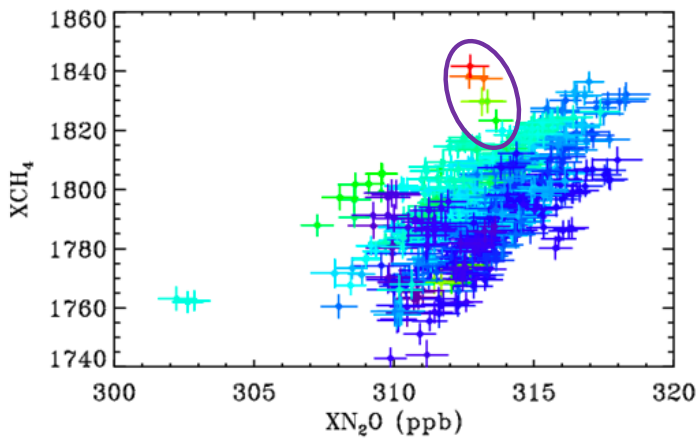
714 **Figure C.1.** HYSPLIT back-trajectories for Nov 10, 2015 (day 314) when the highest ever  $C_2H_6$  was measured from  
 715 JPL. Yellow oval (upper-left) indicates location of Aliso Canyon Underground Storage Facility. Green ball (lower-  
 716 right) denotes JPL, at the convergence of trajectories arriving at 19, 20, & 21 UT. Trajectory calculation used the  
 717 NAM 12 km resolution, hybrid sigma-pressure meteorology. © OpenStreetMap contributors 2020. Distributed under a  
 718 Creative Commons BY-SA License.

719

720 Large  $C_2H_6$  amounts (3x normal) were observed from JPL on Nov 10 (Day 314), but no enhancement of  $C_3H_8$ .  
 721 HYSPLIT back-trajectories for this day indicate that the air arriving at JPL at 1000m above ground was from the  
 722 North-West and had passed over Aliso Canyon USF, confirming that the air over JPL was contaminated by the leak.

Deleted: C

Formatted: Line spacing: 1.5 lines



723



725 **Figure C.2.** Showing the relationship between CH<sub>4</sub> and N<sub>2</sub>O at JPL in 2014–2017 color-coded by C<sub>2</sub>H<sub>6</sub>. Blue points  
726 represent low C<sub>2</sub>H<sub>6</sub> whereas red represents the highest C<sub>2</sub>H<sub>6</sub>. The encircled points represent Nov. 10, 2015, whose  
727 back-trajectory is shown in [the](#) previous figure.

Deleted: C

728 Most of the variation in column CH<sub>4</sub> and N<sub>2</sub>O is associated with the stratospheric circulation. Old airmasses from  
729 high latitude are depleted in CH<sub>4</sub> and N<sub>2</sub>O. To remove these effects, and be able to more clearly see changes driven  
730 by the troposphere, XCH<sub>4</sub> is plotted versus XN<sub>2</sub>O which is similarly affected by stratospheric circulation, but not by  
731 tropospheric emissions. This creates a correlation with the lower-left points representing high-latitude stratospheric  
732 airmasses and the upper right low-latitude airmasses.

733 The encircled points on Fig. C.2 were measured on Nov 10, 2015, when JPL was downwind of the Aliso Canyon  
734 USF leak. The indicate XCH<sub>4</sub> enhancements of over 2%, which probably represent a 10+% enhancement in the  
735 PBL with no enhancement above. There is also a general tendency for higher CH<sub>4</sub> values when C<sub>2</sub>H<sub>6</sub> is elevated on  
736 other days too, as seen from the dark blue points (low C<sub>2</sub>H<sub>6</sub>) being predominantly in the lower right of the figure and  
737 the greener points (higher C<sub>2</sub>H<sub>6</sub>) being located toward the upper left.

Deleted: C

738

#### 739 Code Availability

740 The GFIT code used for the analysis of MkIV spectra is identical to that used by the TCCON project. It is publicly  
741 available under license from the California Institute of Technology for non-commercial use. It can be cloned from:

742 hg clone <https://parkfalls.gps.caltech.edu/tcon/stable/hg/ggg-stable/>  
743 after signing the license agreement and being issued a password.

744

#### 745 Data Availability

746 The ground-based MkIV data used in this paper can be downloaded from two sites:

747 <https://mark4sun.jpl.nasa.gov/ground.html>

748 <ftp://ftp.epc.ncep.noaa.gov/ndacc/station/barcroft/ames/ftir/>

Deleted: K

#### 749 Authors Contributions

750 Toon, Sung, Blavier for data acquisition. Toon and Yu for data interpretation.

#### 751 Competing Interests

752 No competing interests.

#### 753 Acknowledgements

754 The authors gratefully acknowledge the NOAA Air Resources Laboratory (ARL) for the provision of the HYSPLIT  
755 transport and dispersion model and/or READY website (<https://www.ready.noaa.gov>) used in this publication. [We](#)

759 [thank NCEP and GEOS FPIT for their atmospheric analyses.](#) We also acknowledge the NOAA ESRL GMD for  
760 distributing in situ data of C<sub>3</sub>H<sub>8</sub> and C<sub>2</sub>H<sub>6</sub>. We thank NASAs Upper Atmosphere Composition Observation (UACO)  
761 program for funding support.

## 762 **References**

763 Angelbratt, J. et al. Carbon monoxide (CO) and ethane (C<sub>2</sub>H<sub>6</sub>) trends from ground-based solar FTIR measurements  
764 at six European stations, comparison and sensitivity analysis with the EMEP model. *Atmos. Chem. Phys.* **11**,  
765 9253–9269 (2011)

766 Conley, S., G. Franco, I. Faloon, D. R. Blake, J. Peischl, T. B. Ryerson, Methane emissions from the 2015 Aliso  
767 Canyon blowout in Los Angeles. *Science* (2016), 351, (6279), 1317–1320

768 Dalsøren, S.B., Myhre, G., Hodnebrog, Ø. et al. Discrepancy between simulated and observed ethane and propane  
769 levels explained by underestimated fossil emissions, *Nature Geoscience*, **11**, 178–184 (2018).  
770 <https://doi.org/10.1038/s41561-018-0073-0>

771 Franco, B. et al. Retrieval of ethane from ground-based FTIR solar spectra using improved spectroscopy: recent  
772 burden increase above Jungfraujoch. *J. Quant. Spec. Radiat. Trans.* **160**, 36–49 (2015).

773 Franco, B. et al. Evaluating ethane and methane emissions associated with the development of oil and natural gas  
774 extraction in North America. *Environ. Res. Lett.* **11**, 044010 (2016).

775 [Harrison, J.J., Allen, N.D.C., and Bernath, P.F., 2010a, Infrared absorption cross sections for ethane \(C<sub>2</sub>H<sub>6</sub>\) in the 3  
776 μm region, \*Journal of Quantitative Spectroscopy and Radiative Transfer\*, \*\*111\*\*, 357–363,  
777 DOI: 10.1016/j.jqsrt.2009.09.010](#)

778 Harrison, J.J. and Bernath, P.F., 2010b, Infrared absorption cross sections for propane (C<sub>3</sub>H<sub>8</sub>) in the 3 μm  
779 region, *Journal of Quantitative Spectroscopy and Radiative Transfer*, **111**, 1282–1288,  
780 DOI: 10.1016/j.jqsrt.2009.11.027

781 [Helmig, D., Rossabi, S., Hueber, J. et al. Reversal of global atmospheric ethane and propane trends largely due to  
782 US oil and natural gas production. \*Nature Geoscience\*, \*\*9\*\*, 490–495 \(2016\). <https://doi.org/10.1038/ngeo2721>](#)

783 Helmig, D. et al. Climatology and atmospheric chemistry of the non-methane hydrocarbons ethane and propane over  
784 the North Atlantic. *Elementa* **3** (2015).

785 Helmig D., Hueber J., Tans P. (2017), Non-Methane Hydrocarbons from the NOAA ESRL Surface Network, 2004–  
786 2016.

787 [Howard, Touché, Thomas W. Ferrara, Amy Townsend-Small \(2015\), Sensor transition failure in the high flow  
788 sampler: Implications for methane emission inventories of natural gas infrastructure. \*Journal of the Air & Waste  
789 Management Association\*, \*\*65\*\*:7, 856-862, DOI: 10.1080/10962247.2015.1025925](#)

790 Irion, F. W., Gunson, M. R., Toon, G. C., Chang, A. Y., Eldering, A., Mahieu, E., Manney, G. L., Michelsen, H. A.,  
791 Moyer, E. J., Newchurch, M. J., Osterman, G. B., Rinsland, C. P., Salawitch, R. J., Sen, B., Yung, Y. L., and  
792 Zander, R.: Atmospheric Trace Molecule Spectroscopy (ATMOS) Experiment Version 3 data retrievals, *Appl.*  
793 *Opt.*, **41**, 6968–6979, 2002

Deleted: ¶

Formatted: Pattern: Clear (White)

Formatted: Font: (Default) Times New Roman, 10 pt

Formatted: Font: (Default) Times New Roman, 10 pt

Formatted: Font: (Default) Times New Roman, 10 pt

Formatted: Font: (Default) Times New Roman, 10 pt

Formatted: Font: (Default) Times New Roman, 10 pt

Formatted: Font color: Black

795 Rolph, G., Stein, A., and Stunder, B., (2017). Real-time Environmental Applications and Display sYstem: READY.  
796 Environmental Modelling & Software, **95**, 210–228

797 Rosado-Reyes, C. M., and J. S. Francisco (2007), Atmospheric oxidation pathways of propane and its by-products:  
798 Acetone, acetaldehyde, and propionaldehyde, J. Geophys. Res., 112, D14310, doi:10.1029/2006JD007566.

799 Sharpe, Steven W. Johnson, Timothy J. Sams, Robert L. Chu, Pamela M. Rhoderick, George C. Johnson, Patricia  
800 A., "Gas-Phase Databases for Quantitative Infrared Spectroscopy". *Applied Spectroscopy* **58**, 1452-1461, (2004)

801 Stein, A.F., Draxler, R.R, Rolph, G.D., Stunder, B.J.B., Cohen, M.D., and Ngan, F., (2015). NOAA's HYSPLIT  
802 atmospheric transport and dispersion modeling system, Bull. Amer. Meteor. Soc., **96**, 2059-2077

803 Sung, K., G. Toon, A. W. Mantz, and M. A. H. Smith (2013), FTIR measurements of cold C<sub>3</sub>H<sub>8</sub> cross sections at 7–  
804 15 um for Titan atmosphere, *Icarus*, **226**, 1499–1513, doi:10.1016/j.icarus.2013.07.028

805 Toon, G.C., The JPL MkIV Interferometer, *Opt. Photonics News*, **2**, 19–21, 1991

806 Toon, G. C., Blavier, J.-F., Sung, K., Rothman, L. S., and Gordon, I., HITRAN spectroscopy evaluation using solar  
807 occultation FTIR spectra, J. Quant. Spectrosc. Ra., 182, 324–336, <https://doi.org/10.1016/j.jqsrt.2016.05.021>,  
808 2016.

809 Toon, G. C., Blavier, J.-F. L., and Sung, K.: Atmospheric carbonyl sulfide (OCS) measured remotely by FTIR solar  
810 absorption spectrometry, Atmos. Chem. Phys., 18, 1923–1944, <https://doi.org/10.5194/acp-18-1923-2018>,  
811 2018a.

812 Toon, G. C., Blavier, J.-F. L., and Sung, K.: Measurements of atmospheric ethene by solar absorption FTIR  
813 spectrometry, Atmos. Chem. Phys., 18, 5075–5088, <https://doi.org/10.5194/acp-18-5075-2018>, 2018b.

814 Wunch, D., Toon, G. C., Blavier, J.-F. L., Washenfelder, R. A., Notholt, J., Connor, B. J., Griffith, D. W. T.,  
815 Sherlock, V., and Wennberg, P. O.: The total carbon column observing network, Philos. T. R. Soc. A, 369,  
816 2087–2112, <https://doi.org/10.1098/rsta.2010.0240>, 2011.

817 Touché Howard, Thomas W. Ferrara & Amy Townsend-Small (2015) Sensor transition failure in the high flow  
818 sampler: Implications for methane emission inventories of natural gas infrastructure, Journal of the Air & Waste  
819 Management Association, 65:7, 856-862, DOI: 10.1080/10962247.2015.1025925

820 The NEED Project. (2017). Propane [pdf]. Retrieved from  
821 <http://www.need.org/files/curriculum/infobook/propane.pdf>

822 Urbanski, Shawn P., Wei Min Hao and Stephen Baker, Chemical Composition of Wildland Fire Emissions, Chapter  
823 4, Developments in Environmental Science, Volume 8, 79–107, A. Bytnerowicz, M. Arbaugh, A. Riebau, and  
824 C. Andersen (Editors), ISSN: 1474-8177/DOI:10.1016/S1474-8177(08)00004-1

Formatted: Font: Times New Roman, 10 pt

Formatted: Font: 10 pt

<b>Page 5: [1] Deleted</b>	<b>Microsoft Office User</b>	<b>2/9/21 9:46:00 AM</b>
----------------------------	------------------------------	--------------------------



<b>Page 22: [2] Deleted</b>	<b>Microsoft Office User</b>	<b>3/13/21 3:33:00 PM</b>
-----------------------------	------------------------------	---------------------------



<b>Page 23: [3] Deleted</b>	<b>Microsoft Office User</b>	<b>2/4/21 4:24:00 PM</b>
-----------------------------	------------------------------	--------------------------

